Evidence for episodic black hole growth of reionization-era quasars observed with Magellan/FIRE

Leah Bigwood,[1,2]⋆ Anna-Christina Eilers [3] and Robert A. Simcoe[3]

[1]*Department of Physics, Durham University, South Road, Durham DH1 3LE, UK*
[2]*Institute of Astronomy, University of Cambridge, Madingley Road, Cambridge CB3 OHA, UK*
[3]*MIT Kavli Institute for Astrophysics and Space Research, 77 Massachusetts Avenue, Cambridge, MA 02139, USA*

ABSTRACT

Observations of high-redshift quasars hosting billion solar mass black holes at $z \gtrsim 6$ challenge our understanding of early supermassive black hole (SMBH) growth. In this work, we conduct a near-infrared spectroscopic study of 19 quasars at $6.2 \lesssim z \lesssim 7.5$, using the Folded-port InfraRed Echellette instrument on the 6.5-m Magellan/Baade Telescope. We estimate the single-epoch masses of the quasars' SMBHs by means of the Mg II emission line and find black hole masses of $M_{\rm BH} \approx (0.2\text{–}4.8) \times 10^9$ $M_\odot$. Furthermore, we measure the sizes of the quasars' proximity zones, which are regions of enhanced transmitted flux bluewards of the Ly α emission line, ionized by the quasars' radiation itself. While it has been shown that the proximity zone sizes correlate with the quasars' lifetimes due to the finite response time of the intergalactic medium to the quasars' radiation, we do not find any correlation between the proximity zone sizes and the black hole mass, which suggests that quasar activity and the concomitant black hole growth are intermittent and episodic.

Key words: methods: data analysis – quasars: emission lines – quasars: supermassive black holes.

1 INTRODUCTION

Quasars are the most luminous, non-transient sources in the observable Universe, and thus they have been observed well into the epoch of reionization. To date, more than 200 quasars above a redshift of $z \gtrsim 6$ have been discovered (Fan, Banados & Simcoe 2022), with the current redshift record holder at $z = 7.64$ (Wang et al. 2021), which is at a time when the universe is only ≈ 700 Myr old. It is well established that their emission is powered by the accretion of material on to a central supermassive black hole (SMBH) from the surrounding accretion disc (e.g. Salpeter 1964; Lynden-Bell 1969; Kormendy & Richstone 1995; Richstone et al. 1998). Analyses of the quasars' rest-frame ultraviolet (UV) and optical spectra, including those discovered in the reionization era, have demonstrated that the quasars host SMBHs with masses exceeding $M_{\rm BH} \sim 10^9$ $M_\odot$ (e.g. Mortlock et al. 2011; Mazzucchelli et al. 2017; Eilers et al. 2020).

The existence of billion solar mass SMBHs at high redshifts challenges our understanding of black hole growth due to the short amount of cosmic time available to reach such masses. It has been argued that in order to grow such SMBHs from a constant supply of fuelling material, the stellar remnant seeds must have masses of the order of $M_{\rm BH} \sim 100$ $M_\odot$ and quasar activity of the order of $t_Q \sim 10^9$ yr, i.e. when the SMBH's active accretion is powering the quasar's UV luminosity, is required, even if accretion is continuous at the Eddington limit (Volonteri 2012). Given that this time is comparable to the age of the Universe for quasars observed at $z > 6$, constraining the time-scale that quasars are active is imperative to understanding

whether these objects exacerbate the challenges in the theory of SMBH formation and growth.

However, measuring the time-scales of quasar activity has proven to be challenging, even for objects at lower redshift. At $z \sim 2\text{–}4$, weak constraints of $t_Q \sim 10^6\text{–}10^9$ yr have been obtained by means of the spatial clustering of quasars and the inferred abundance of their host dark matter haloes. This relies on the idea that rarer objects tend to be highly biased tracers of the underlying dark matter distribution. Therefore, a comparison of the number density of quasars to the abundance of their host dark matter haloes provides an estimate of the duty cycle of luminous quasars (e.g. Haiman & Hui 2001; Martini & Weinberg 2001). A further study of local early-type galaxies by Yu & Tremaine (2002) constrained $t_Q \sim (3\text{–}13) \times 10^7$ yr, which was estimated under the assumption that if black hole growth predominantly takes place during optically bright quasar phases, the quasar luminosity function should be reflective of the gas accretion history of local black holes. Spectroscopic studies have also provided additional constraints by detecting changes in quasar luminosities, and therefore ionization rates, and the time lag to the resulting change in the intergalactic medium (IGM)'s opacity. This method has resulted in estimates in the range of $t_Q \sim 10^5\text{–}10^7$ yr (e.g. Adelberger 2004). Tighter constraints on the time-scale of quasar activity, and estimates for the objects at higher redshift that challenge current SMBH formation theory, are clearly necessary to progress our understanding.

For quasars at $z \gtrsim 5.5$, it has been shown that time-scales of their nuclear activity can be estimated by means of the size of their 'proximity zones' (see e.g. Eilers et al. 2017, 2021; Davies, Hennawi & Eilers 2019). Quasars ionize the surrounding IGM, which leads to a deficit of neutral hydrogen and therefore reduced Ly α

⋆ E-mail: lmb224@cam.ac.uk

absorption. This results in a region of enhanced transmitted flux in quasar spectra occurring immediately bluewards of the Ly α emission line. Due to the finite response time of the IGM to the ionizing radiation, the size of this region has a dependence on the amount of time the quasar has been active. At $z \sim 6$, the recombination time of the IGM to become sufficiently neutral to be opaque to Ly α photons is short, and thus the proximity zone sizes only reflect the time of the last accretion episode. The situation changes with increasing redshift; at $z \gtrsim 7$, the epoch of reionization is not yet complete and therefore the IGM is increasingly neutral. This complicates the mapping from proximity zone size to lifetime, with the integrated lifetime being measured as opposed to an individual episode. The spectra of quasars in highly neutral IGM exhibit a damping wing on the Ly α emission line predominantly due to the intrinsic line width and the velocity dispersion of atoms (Miralda-Escudé 1998; Simcoe et al. 2012; Davies, Hennawi & Eilers 2019). The damping wing has thus far only been observed in objects at $z > 7$ (e.g. Greig et al. 2017; Davies et al. 2018; Yang et al. 2020). In this work, we measure the proximity zone sizes of objects at $z < 7$, where we expect the IGM to already be mostly ionized. As a result, we hereinafter define the 'lifetime' of a quasar as the time elapsed since the *current* luminous phase began, since this is the time-scale the proximity zone size of $z \lesssim 7$ quasars is sensitive to.

Previous studies of the proximity zones of observed reionization-era quasars have resulted in lifetime estimates to be as short as $t_Q < 10^4$ yr (Eilers et al. 2021) with an average quasar lifetime of $t_Q \sim 10^6$ yr (Morey et al. 2021). If SMBH growth occurs in a single episode and only when the quasar is optically bright, this poses the question of whether they form from more massive initial seeds, or whether the accretion could happen in a radiatively inefficient manner. The simple exponential light curves in which a quasar emits at a constant luminosity throughout its entire lifetime, so-called light-bulb light curves, of quasars have also been questioned, and in reality quasars may undergo multiple episodes of luminous quasar activity with concurrent black hole growth, alternated with quiescent phases (e.g. Novak, Ostriker & Ciotti 2011; Schawinski et al. 2015; Davies, Hennawi & Eilers 2020). This behaviour has been demonstrated in hydrodynamical simulations, with episodic quasar lifetimes and intermittent black hole growth being observed in works such as Novak, Ostriker & Ciotti (2011). A more complete sample of masses and lifetimes for high-redshift quasars is clearly required in order to address these possibilities of their formation and growth.

In this paper, we carry out a spectroscopic study of 19 quasars at $6.17 < z < 7.51$. At these redshifts, the rest-frame UV emission is shifted to the near-infrared (NIR) wavelengths; hence, we utilize the capabilities of the Folded-port InfraRed Echellette (FIRE) instrument on the Magellan/Baade Telescope to obtain NIR spectra of these quasars. We measure the sizes of proximity zones for the quasars at $z < 7$, noting that we leave the modelling of the damping wing signature for the highest redshift objects for a companion paper (Ďurovčíková et al. 2024). We also estimate the single-epoch masses of the host SMBH of all quasars in the sample by means of the Mg II line. By testing for correlation between these two measurements, we suggest that quasar activity is episodic and intermittent, and discuss obscured growth as a resolution to the tension with SMBH formation and growth models.

Our paper is structured as follows: Section 2 introduces the quasar sample and the data reduction procedure. In Section 3.1, we obtain single-epoch SMBH mass estimates, as well as redshifts derived from the Mg II line. We then determine the continuum emission of each quasar in the Ly α forest in Section 3.2, which is required

Table 1. Observational information for the quasars in our sample, as well as the best redshift estimate available in the literature. We also list the absolute magnitudes M_{1450} for the subset of quasars for which this is required to correct the proximity zone measurement (see Section 3.3).

Object	z	M_{1450}	Date	t_{exp} (s)
J0020−3653	6.834 ± 0.001^d	−26.92	Jan 2021	3600
			June 2021	14 400
			Oct 2021	10 800
J0216−5226	6.41 ± 0.05^g	−25.19	Jan 2021	9600
J0218+0007	6.7700 ± 0.0013^c	−25.55	Jan 2021	7200
			Dec 2021	9000
J0244−5008	6.724 ± 0.001^b	−26.72	Jan 2021	4800
			Sept 2021	7200
			Oct 2021	10 800
			Jan 2022	9000
J0252−0503	7.0006 ± 0.0009^c	–	Jan 2021	5400
			Sept 2021	2400
J036+03	6.5412 ± 0.0018^f	−27.4	Aug 2022	7200
J0319−1008	6.8275 ± 0.0021^c	−25.36	Oct 2021	16 200
J0410−4414	6.21 ± 0.01^b	−26.14	Jan 2021	4800
J0411−0907	6.8260 ± 0.0007^c	−26.58	Nov 2021	15 600
J0525−2406	6.5397 ± 0.0001^c	−25.47	Dec 2021	10 800
J0910+1656	6.7289 ± 0.0005^c	−25.34	Mar 2021	12 600
J0921+0007	6.5646 ± 0.0003^c	−25.19	Jan 2021	7200
			Apr 2021	4800
J1007+2115	7.5149 ± 0.0004^c	–	Jan 2021	14 400
			Mar 2021	7200
			Apr 2021	7200
J1104+2134	6.7662 ± 0.0009^c	−26.63	Jan 2021	9600
			Mar 2021	5400
			Apr 2021	9600
			June 2021	6000
J1217+0131	6.17 ± 0.05^e	−25.76	June 2021	13 200
J1526−2050	6.5864 ± 0.0005^a	−27.20	July 2021	9600
			Apr 2022	13 800
J1535+1943	6.370 ± 0.001^c	–	Apr 2021	8400
J2002−3013	6.6876 ± 0.0004^c	−26.9	Mar 2021	10 200
			Apr 2021	4800
			July 2021	4200
J2102−1458	6.6645 ± 0.0002^c	−25.53	Apr 2021	4800

^{a}Decarli et al. (2018).
^{b}Reed et al. (2017).
^{c}Yang et al. (2021).
^{d}Reed et al. (2019).
^{e}Wang et al. (2017).
^{f}Bañados et al. (2015). ^{g}Yang et al. (2019).

for the proximity zone measurements shown in Section 3.3. We go on to discuss the implications of our results on quasar lifetimes and SMBH growth in Section 4. We summarize our findings in Section 5. Throughout the manuscript, we assume a flat Lambda cold dark matter cosmology ($h = 0.677$, $\Omega_\mathrm{m} = 0.307$) consistent within the 1σ results of Planck Collaboration XIII (2016).

2 QUASAR SAMPLE

The quasar sample contains 19 quasars at $6.2 \lesssim z \lesssim 7.5$ totalling more than 83 h of observations with the FIRE instrument on the 6.5-m Magellan/Baade Telescope, which were conducted between 2021 January and 2022 August. All observations are obtained in Echelle mode using a 0.6 arcsec slit. The details of the observations are shown in Table 1.

The spectra are homogeneously reduced using the open-source PYTHON-based spectroscopic data reduction pipeline PYPEIT[1] version 1.7.1 (Prochaska et al. 2020a). The details of this pipeline are described in Prochaska et al. (2020b), but we will summarize them here briefly. In short, we obtain an on-sky wavelength solution based on sky OH lines, and perform the sky subtraction on the 2D images by differencing exposures dithered along the slit. We fit a *b*-spline to further eliminate sky line residuals following Bochanski et al. (2009). We then perform an optimal extraction (Horne 1986) to obtain the 1D spectra. All spectra are flux calibrated using sensitivity functions of standard stars, ideally observed during the same night.

We co-add the flux-calibrated 1D spectra from each night and correct for telluric absorption features by jointly fitting an atmospheric model and a quasar model. The telluric model grids are produced using the Line-By-Line Radiative Transfer Model (Clough et al. 2005).

All reduced spectra are shown in Fig. 3.

The best published redshift estimates for the majority of these quasars are derived from the [C II] 157.74 μm emission line. When this is not available, the systematic redshifts are traced by the Mg II emission line or the extended Ly α emission. Table 1 lists the best redshift estimates in the literature.

3 ANALYSIS

3.1 Black hole mass estimates

Under the assumption that the gravitational pull of the central black hole dominates the dynamics in the broad-line region (BLR) of the quasar, we can apply the virial theorem. This allows an estimation of the black hole mass to be obtained by means of the width of the broad emission lines arising from the gas in the BLR and the luminosity output. We utilize the black hole mass scaling relation of Vestergaard & Osmer (2009), i.e.

$$\frac{M_{\mathrm{BH}}}{M_{\odot}} = 10^{6.86} \left(\frac{\mathrm{FWHM}_{\mathrm{Mg\,II}}}{10^3 \ \mathrm{km\,s}^{-1}} \right)^2 \left(\frac{\lambda L_{\lambda,\,3000\,\text{\AA}}}{10^{44} \ \mathrm{erg\,s}^{-1}} \right)^{0.5}, \qquad (1)$$

which was calibrated to the existing H β and C IV scaling relations using several thousand high-quality quasar spectra from Sloan Digital Sky Survey (SDSS) Data Release 3 quasar sample ranging $0.08 < z <$ 5.41. The intrinsic 1σ scatter in the scaling relation is approximately 0.55 dex.

We model the quasar emission in the spectral region 2100 Å $\leq$ $\lambda_{\mathrm{rest}} \leq$ 3088 Å as a superposition of a power-law continuum with slope α arising from the accretion disc, a scaled template spectrum of the iron emission lines Fe II and Fe III in the BLR, and a single Gaussian of variance $\sigma_{\mathrm{Mg\,II}}^2$ centred on $\mu_{\mathrm{Mg\,II}}$ to model the Mg II line, i.e.

$$f_\lambda = a_0 \left(\frac{\lambda}{2500} \right)^{-\alpha} + a_1 f_{\lambda,\,\mathrm{iron}} + a_2 \exp \left[-\frac{(\lambda - \mu_{\mathrm{Mg\,II}})^2}{2\sigma_{\mathrm{Mg\,II}}^2} \right], \qquad (2)$$

where a_0, a_1, and a_2 are the amplitudes of the individual components. We use the iron template spectrum of Tsuzuki et al. (2006), which was derived from a narrow emission line quasar. We note that we utilize the template of Tsuzuki et al. (2006) over Vestergaard & Wilkes (2001), since the former separates the Mg II emission from the underlying Fe II emission, whereas the latter sets the Fe II emission

to zero in the region of the Mg II line. This resulted in the model of the quasar emission around the Mg II line showing a better quality of fit to the spectra in our sample. We, however, caveat that the Vestergaard & Osmer (2009) scaling relation was constructed using the iron template of Vestergaard & Wilkes (2001), and that Schindler et al. (2020) demonstrated that using the Tsuzuki et al. (2006) template with this scaling relation can bias SMBH masses low by ∼0.21 dex. To mimic the broad emission lines present in our quasars' spectra, we convolve the iron template with a Gaussian kernel of width FWHM ≈ FWHM$_{\mathrm{Mg\,II}}$, where FWHM refers to full width at half-maximum. Prior to fitting the model, we rescale the reduced spectrum so that the integrated flux within the *J* band is in agreement with the reported magnitude, *J*-band magnitude in the literature, if available.

By means of the Markov chain Monte Carlo sampler EMCEE (Foreman-Mackey et al. 2013), we estimate the free parameters of the model assuming flat priors and adopt the mean of the posterior probability distribution as the best parameter estimate. The continuum luminosity at $\lambda_{\mathrm{rest}} = 3000$ Å was determined by estimating the flux at $\lambda = 3000$ Å from the best-fitting power-law continuum. The best fits to the Mg II emission lines for each quasar in our sample are displayed in Fig. 1, and the corresponding mass estimates are listed in Table 2.

We measure the quasar redshift derived from the Mg II emission line $z_{\mathrm{Mg\,II}}$ using the estimations of the Gaussian centre, $\mu_{\mathrm{Mg\,II}}$. Note that this emission does not arise from the host galaxy (unlike the [C II] line), and instead originates in the BLR. As a result, the emission may experience modest velocity shifts with respect to the systematic redshift of the quasar. The average shift with respect to the quasar's systematic redshift is $\Delta v(\mathrm{Mg\,II} - [\mathrm{C\,II}]) = 391 \ \mathrm{km\,s}^{-1}$ (Schindler et al. 2020). The $z_{\mathrm{Mg\,II}}$ estimates are listed in Table 2. We note that we measure the Mg II derived redshift of J0216−5226 to be $z_{\mathrm{Mg\,II}} = 6.3283 \pm 0.0094$, which is blueshifted from the best available literature estimate of $z = 6.41 \pm 0.05$ (Yang et al. 2019) by ∼3305 km s^{-1}. Yang et al. (2019) attained the measurement by matching quasar template spectra to the Ly α and N V emission lines, noting that the offset of the Ly α line with respect to the systematic redshift is typically $\Delta v(\mathrm{Ly}\,\alpha - [\mathrm{C\,II}]) \sim 500 \ \mathrm{km\,s}^{-1}$. We therefore find that the estimated $z_{\mathrm{Mg\,II}}$ for this object exhibits a blueshift in significant excess to the typical systematic velocity offset.

Several quasars in our sample overlap with those characterized previously in Yang et al. (2021). Fig. 2 compares the respective mass estimates obtained, finding overall a reasonable agreement between the two studies within the intrinsic scatter of the scaling relation.

3.2 Quasar continuum

In order to measure the proximity zone, we first require an estimate for the quasar continuum emission in the Ly α forest. Residual neutral hydrogen present in the IGM leads to significant absorption bluewards of the Ly α emission line for the spectra of high-redshift quasars.

We obtain the continuum estimate using a principal component analysis (PCA; e.g. Suzuki et al. 2005; Pâris et al. 2011; Davies et al. 2018). Due to the absorption bluewards of Ly α, we only fit to the 'red' side of the spectra (1220 Å $< \lambda_{\mathrm{rest}} <$ 2850 Å), and then predict the continuum emission on the 'blue' side (1181 Å $< \lambda_{\mathrm{rest}}$ $<$ 1220 Å). The 'red' and 'blue' PCA components, R_i and B_i, are a set of 10 and 6 basis spectra, respectively, obtained with a PCA decomposition of 12 764 training spectra from the SDSS Baryon Oscillation Spectroscopic Survey sample into an orthogonal basis (Davies et al. 2018).
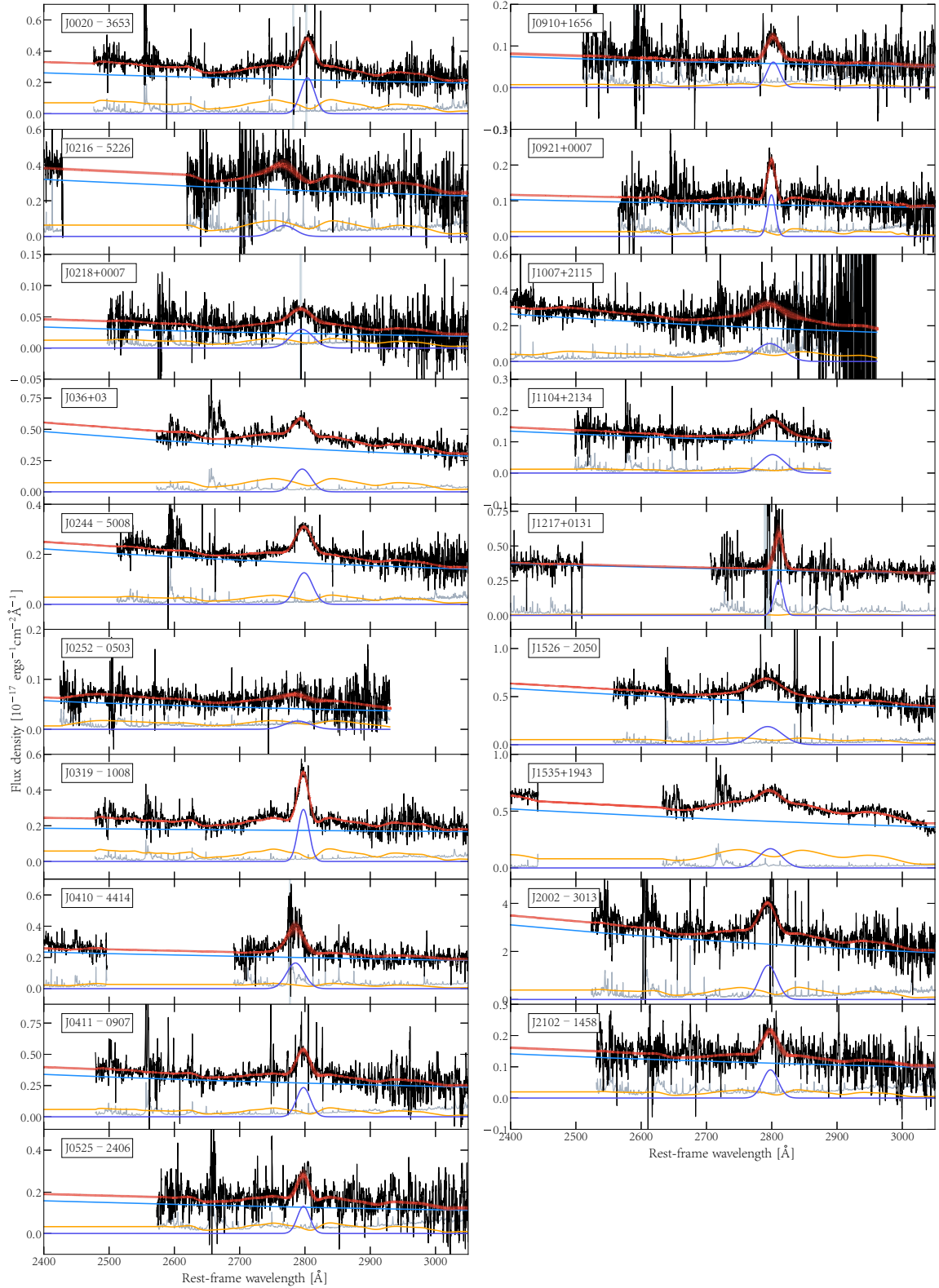

Figure 1. The multicomponent fits to the spectral region around the Mg II emission line, shown in the quasars' rest frame using the best redshift estimate. The spectrum and its noise vector have been smoothed with a boxcar function of width 10 pixels, and are shown in black and grey, respectively. Regions of strong telluric absorption were removed, and further masking was applied to broad absorption lines and noisy spikes, shown by the shaded grey areas. The faint red curves show 100 draws from the posterior distribution of the best-estimate model. The individual components are shown as the coloured curves: a power-law continuum (blue curve), the iron template spectrum broadened to mimic the emission from the BLR (yellow curve), and a Gaussian to model the Mg II emission line (purple curve).

Table 2. The columns show the name of the quasar, the best published redshift z, the measured uncorrected and magnitude-corrected proximity zone sizes, R_p and $R_{p, corr}$, redshift estimates based on the Mg II emission line $z_{Mg II}$, and mass estimates M_{BH}.

Object	z	R_p (pMpc)	$R_{p, corr}$ (pMpc)	$z_{Mg II}$	$FWHM_{Mg II}$ (Å)	L_{3000} (10^{43} erg s^{-1} Å^{-1})	M_{BH} (10^9 M$_\odot$)
J0020−3653[a]	6.8340 ± 0.0010	1.70 ± 0.25	1.75 ± 0.26	6.8485 ± 0.0007	2727 ± 80	0.883 ± 0.008	0.88 ± 0.05
J0216−5226	6.4100 ± 0.0500	–	–	6.3288 ± 0.0098	4260 ± 936	0.837 ± 0.014	2.08 ± 0.92
J0218+0007	6.7700 ± 0.0013	1.17 ± 0.48	2.07 ± 0.84	6.7600 ± 0.0028	4350 ± 273	0.085 ± 0.003	0.69 ± 0.09
J0244−5008[a]	6.7240 ± 0.0010	2.14 ± 0.28	2.39 ± 0.31	6.7240 ± 0.0007	3272 ± 78	0.609 ± 0.005	1.05 ± 0.05
J0252−0503	7.0006 ± 0.0009	–	–	6.9732 ± 0.0099	4905 ± 902	0.167 ± 0.006	1.24 ± 0.46
J0319−1008[a]	6.8275 ± 0.0021	1.26 ± 0.16	2.39 ± 0.31	6.8246 ± 0.0005	2150 ± 47	0.742 ± 0.008	0.50 ± 0.02
J036+03[a]	6.5412 ± 0.0018	3.20 ± 0.47	2.74 ± 0.40	6.5334 ± 0.0012	3480 ± 118	1.135 ± 0.009	1.62 ± 0.11
J0410−4414[a]	6.2100 ± 0.0100	3.00 ± 0.92	4.21 ± 1.29	6.1759 ± 0.0022	3439 ± 332	0.602 ± 0.008	1.15 ± 0.22
J0411−0907	6.8260 ± 0.0007	3.68 ± 0.25	4.34 ± 0.30	6.8233 ± 0.0016	2686 ± 174	1.071 ± 0.015	0.94 ± 0.12
J0525−2406	6.5397 ± 0.0001	1.53 ± 0.04	2.79 ± 0.07	6.5372 ± 0.0022	2384 ± 200	0.438 ± 0.012	0.47 ± 0.08
J0910+1656	6.7289 ± 0.0005	0.89 ± 0.18	1.71 ± 0.35	6.7391 ± 0.0024	2517 ± 236	0.218 ± 0.008	0.37 ± 0.07
J0921+0007	6.5646 ± 0.0003	1.97 ± 0.11	4.01 ± 0.23	6.5669 ± 0.0008	1561 ± 87	0.321 ± 0.006	0.17 ± 0.02
J1007+2115	7.5149 ± 0.0004	–	–	7.5099 ± 0.0079	5376 ± 704	0.947 ± 0.025	3.53 ± 0.93
J1104+2134	6.7662 ± 0.0009	3.46 ± 0.33	4.00 ± 0.38	6.7731 ± 0.0018	4592 ± 205	0.391 ± 0.005	1.65 ± 0.15
J1217+0131[a]	6.1700 ± 0.0500	3.74 ± 0.88	6.08 ± 1.43	6.2002 ± 0.0021	1717 ± 186	0.981 ± 0.009	0.37 ± 0.08
J1526−2050	6.5864 ± 0.0005	3.50 ± 0.19	3.23 ± 0.18	6.5729 ± 0.0014	5530 ± 136	1.559 ± 0.010	4.79 ± 0.24
J1535+1943	6.3700 ± 0.0010	–	–	6.3681 ± 0.0014	4375 ± 140	1.301 ± 0.006	2.74 ± 0.18
J2002−3013	6.6876 ± 0.0004	3.73 ± 0.15	3.88 ± 0.15	6.6764 ± 0.0011	3373 ± 99	8.285 ± 0.073	4.11 ± 0.24
J2102−1458	6.6645 ± 0.0002	2.41 ± 0.07	4.28 ± 0.13	6.6625 ± 0.0027	3001 ± 241	0.410 ± 0.009	0.72 ± 0.12

[a]Objects for which the redshift estimate based on the Mg II emission line, $z_{Mg II}$, derived in this work is an improvement on the best published redshift z.
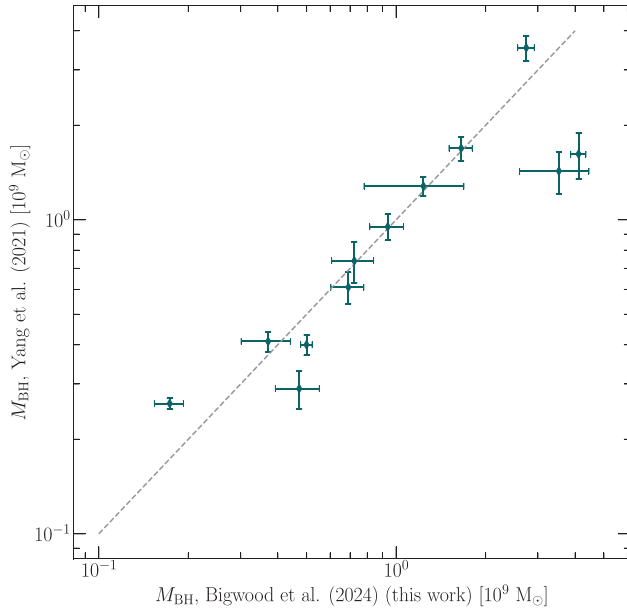
Figure 2. Comparing the masses of host SMBHs estimated in this paper to those obtained in Yang et al. (2021), for the quasars that are characterized in both works. The error bars displayed are purely statistical. There is an intrinsic systematic scatter in M_{BH} of approximately 0.55 dex arising from the scaling relation of Vestergaard & Osmer (2009).

We obtain the rest-frame quasar spectra using the best available redshift estimate, i.e. taking those derived from the Mg II emission line in Section 3.1 if it improves upon the best previously published redshift estimate. We mask spectral regions with significant atmospheric absorption, and normalize the spectra to unity in a region free of significant emission lines at 1290 ± 2.5 Å. To remove strong metal absorption lines from intervening absorption systems along our line of sight, we then fit a spline to the 'red' region of the spectra, and remove outlying values by sigma clipping at the 3σ level. We use

EMCEE to estimate the 10 PCA coefficients for these components in the 'red' spectral region, r_i, thus estimating the quasar continuum in the logarithmic flux space as

$$\log f_\lambda \approx \langle \log f_\lambda \rangle + \sum_{i=1}^{10} r_i R_i, \tag{3}$$

where $\langle \log f_\lambda \rangle$ is the mean logarithmic flux. We also fit for a redshift offset Δz, to account for offsets between the broad emission lines and the systemic redshift. We chose flat priors for each free parameter, taking the 5σ region for r_i from the training set data (see Davies et al. 2018, for details) and $\Delta z \in [-0.15, 0.03]$. We adopt the mean of the resulting posterior probability distribution as the best parameter estimate.

The best-estimate r_i are then projected on to the coefficients of the blue PCA components, b_j, using a projection matrix $P_{i,j}$ also determined from the training spectra, i.e.

$$b_j = \sum_{i=0}^{10} r_i P_{i,j}. \tag{4}$$

We thus obtain a fit for the quasar continua over the entire spectral region 1181 Å $< \lambda_{rest} <$ 2850 Å. Fig. 3 presents the continua estimates for the 19 quasars in our sample. In Fig. A1, we enlarge the region showing the continuity of the red and blue continuum reconstruction components in order to better demonstrate the quality of the continuum reconstruction.

Note that J1535+1943 is heavily dust obscured, leading to an unusual continuum slope. Hence, we caution that the continuum estimate might be biased due to the lack of similar objects in the PCA training set. It would be interesting to measure the proximity zone size and infer the quasar lifetime for this obscured object; however, simultaneous modelling of the quasar continuum and the obscuration rate would be required. We therefore do not take this object into account in the proximity zone analysis of the following section and leave a full study of it for future work.
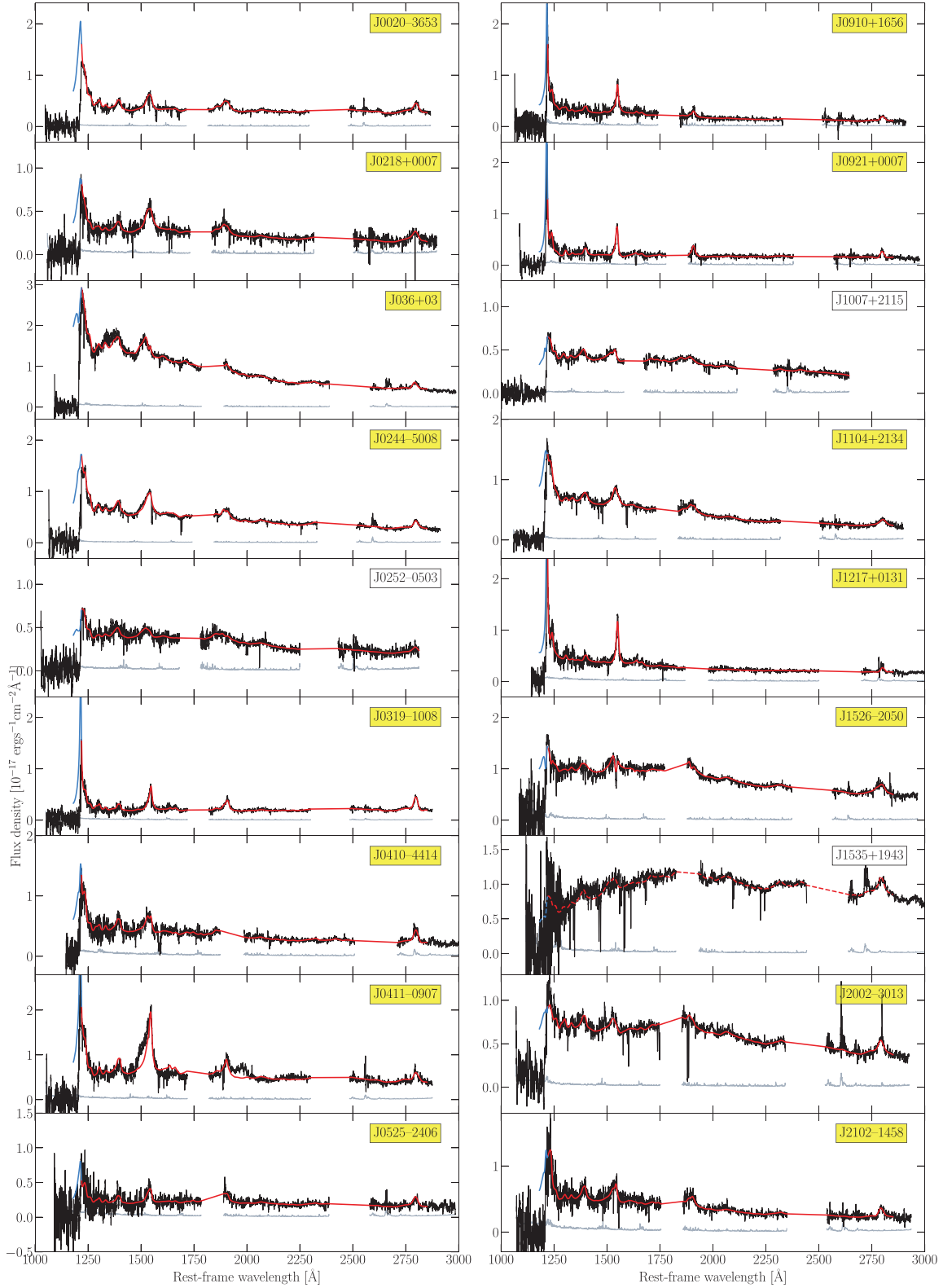
Figure 3. The spectra and best-fitting continua model of the 19 quasars in our sample. We estimate the continua across the full spectral range by fitting 10 'red' principal components to the region 1220 Å $< \lambda_{\mathrm{rest}} <$ 2850 Å (red curve), and projecting on to a set of 6 'blue' principal components covering 1181 Å $<$ $\lambda_{\mathrm{rest}} <$ 1220 Å (blue curve). A boxcar smoothing of 20 pixels has been applied to the spectrum (black) and its noise vector (grey). We have removed regions of strong telluric absorption, and further masking was applied to broad absorption lines and regions of high noise, shown by the shaded grey areas. Labels in yellow denote objects for which we use the continuum reconstruction in the proximity zone analysis of Section 3.3. For these objects, we enlarge the region showing the continuity between the red and blue continuum reconstruction components in Fig. A1. We show the continua model of J1535+1943 as a dashed curve due to its highly usual slope resulting from dust obscuration.

3.3 Measuring proximity zone sizes

We adopt the standard definition of the proximity zone used in previous studies (e.g. Fan et al. 2006; Carilli et al. 2010; Eilers et al. 2020; Satyavolu et al. 2023b). We normalize the rest-frame quasar spectra by the continuum estimate, and apply a boxcar smoothing to the normalized flux of width 20 Å in the observed wavelength frame. At $z = 6$, this smoothing scale corresponds to approximately 1 pMpc or 700 km s^{-1}. The extent of the proximity zone, R_p, is defined as the region bluewards of the Ly α emission line before the smoothed transmitted flux drops below 10 per cent. This follows the standard definition first adopted by Fan et al. (2006), and utilized in other previous studies (e.g. Willott et al. 2007; Eilers et al. 2017; Mazzucchelli et al. 2017). In Fig. 4, we present the smoothed continuum-normalized spectrum and show the extents of the proximity zone sizes for our quasar sample. Note that damping wings in quasar spectra have been detected in objects at $z > 7$, imprinted by the high neutral fraction of the IGM (Wang et al. 2020; Yang et al. 2020). As a result, we exclude proximity zone estimates for objects at $z > 7$, since they would require careful modelling of the neutral gas fraction in the proximity zone size, as shown in previous work (e.g. Greig et al. 2017; Davies et al. 2019).

The extents of the proximity zones are dependent on the luminosity of the quasar, since a more luminous quasar will create more ionizing radiation. Thus, we also calculate the luminosity-corrected proximity zone size, $R_{p, corr}$, which has been shown to correlate with the quasar's lifetime (e.g. Eilers et al. 2017, 2020; Morey et al. 2021). We adopt the relation to eliminate the luminosity dependence introduced in Eilers et al. (2017):

$$R_{p,\,corr} = R_p \times 10^{-0.4(-27-M_{1450})/2.35}, \tag{5}$$

which normalizes all proximity zone measurements to an absolute magnitude of $M_{1450} = -27$. Table 2 records both the measured and magnitude-corrected proximity zone sizes for our set of quasars.

4 DISCUSSION

To date, over 100 Mg II-based SMBH mass estimates have been obtained for quasars at $z > 5.9$ (Fan et al. 2023). Previous studies such as Yang et al. (2021), Farina et al. (2022), and Mazzucchelli et al. (2023) report SMBH masses in the range of $\sim(0.3-12.6) \times 10^9$ M$_\odot$ for quasars observed in the late stages of cosmic reionization. The mass estimates derived in this work lie within $M_{BH} \approx (0.2-4.8) \times 10^9$ M$_\odot$, and are thus broadly consistent with those reported in the literature. We note that our sample does not include some of the heaviest SMBHs reported in the literature exceeding $M_{BH} \gtrsim 10^{10}$ M$_\odot$ (Wu et al. 2015; Mazzucchelli et al. 2023).

For quasars at $z > 5.7$, proximity zone sizes have thus far been measured in 87 objects. Satyavolu et al. (2023b) recently presented a study of 22 quasars at $5.8 < z < 6.6$ and inferred proximity zones in the range of $R_p \sim 2-7$ pMpc. Eilers et al. (2017) discovered three quasars with exceptionally small proximity zones of $R_{p, corr} < 2$ pMpc, with Eilers et al. (2020) finding a further four objects that meet these criteria. After considering patchy reionization and proximate absorbers as causes for a potential truncation of the proximity zone, they conclude that the most compelling explanation for the extremely small proximity zone sizes is quasar lifetimes as short as $t_Q < 10^5$ yr. In this study, we measure luminosity-corrected proximity zones in the range of $R_{p, corr} \approx 1.7-6.1$ pMpc, consistent with the previous measurements in the literature. We find two objects (J0020−3653 and J0910+1656) with small proximity zones of $R_{p, corr} < 2$ pMpc, potentially indicative of very young objects. In a companion paper, we obtain precise lifetime estimates for the quasars in our sample (Ďurovčíková et al. 2024) to study their SMBH growth phases.

It is known that the sizes of proximity zones are correlated with quasars' UV luminous lifetimes, during which the black hole growth occurs (e.g. Salpeter 1964; Soltan 1982; Khrykin et al. 2016; Eilers et al. 2017; Davies et al. 2020). With this in mind, if quasars were to have only one accretion episode, i.e. a duty cycle of unity, and similar initial black hole seeds, we would expect to find a correlation between proximity zone size and black hole mass. In Fig. 5, we test this scenario by showing the estimated SMBH masses against the luminosity-corrected proximity zone sizes. We find a Pearson correlation coefficient of $r = 0.054$, indicating no correlation between the two measurements. This suggests that SMBHs likely grow in multiple accretion episodes and that quasar light curves do not follow a simple light-bulb model, as has been suggested in previous studies (e.g. Novak et al. 2011; Schawinski et al. 2015; Davies et al. 2020; Satyavolu et al. 2023a). However, short accretion episodes as implied by the small proximity zones measured in quasars at $z \approx 6$ (e.g. Eilers et al. 2021) do not alleviate, and in fact aggravate, the challenge of growing billion solar mass black holes by $z \sim 6$. Recently, Satyavolu et al. (2023a) proposed the solution that quasars may undergo phases of obscured growth, when the black hole grows without emitting optical radiation along a given sightline. By allowing black hole growth when the quasar is not optically bright, they demonstrated that super-Eddington accretion is not necessarily a requirement of achieving the black hole masses we observe at high redshift. This behaviour has also been displayed in hydrodynamical simulations, with Bennett et al. (2024) showing that simulated quasars hosting $\sim 10^9$ M$_\odot$ black holes at $z = 6$ spend a significant amount of time with sightlines obscured in the UV, as a result of surrounding dust and gas. Obscured growth therefore provides a potential reconciliation between the short proximity zone sizes and host SMBH masses measured for high-redshift quasars, thus aiding the tension in black hole formation and growth models.

It is important to note that our conclusions rely on the correlation between proximity zone size and lifetime, which assumes that the quasars we measure at $z < 7$ reside in an ionized IGM. Although we do not detect the damping wing signature of a neutral IGM in our sample, we cannot rule out the possibility that patches of neutral hydrogen are still present around the quasars at $z > 6$. Future work will, however, account for this by modelling the reionization of the IGM and attaining robust measurements of quasar lifetimes, better informing us on the theories we have suggested.

5 SUMMARY

In this work, we present a new high-redshift quasar sample obtained with FIRE on the 6.5-m Magellan/Baade Telescope. All spectra, observed over more than 83 h, are reduced homogeneously using the pipeline PYPEIT version 1.7.1. We estimate the black hole masses of this quasar set, and demonstrate that each hosts a billion solar mass SMBH, as expected from previous high-z quasar studies. We also measure the proximity zone sizes of this quasar sample, since they are known to correlate with the UV luminous quasar lifetimes. We do not find a correlation between the luminosity-corrected proximity zone sizes and black hole masses, which suggests that quasar activity is episodic and intermittent.

Future work will include detailed modelling of the quasars' proximity zones, including the damping wing signature. This will allow robust estimates of the quasars' lifetimes to be derived, in addition to the neutral fraction of the IGM. Obtaining lifetime measurements will enable us to study the dependence with black hole mass more robustly. We note, however, that given the lack of correlation between proximity zone size and black hole mass found in
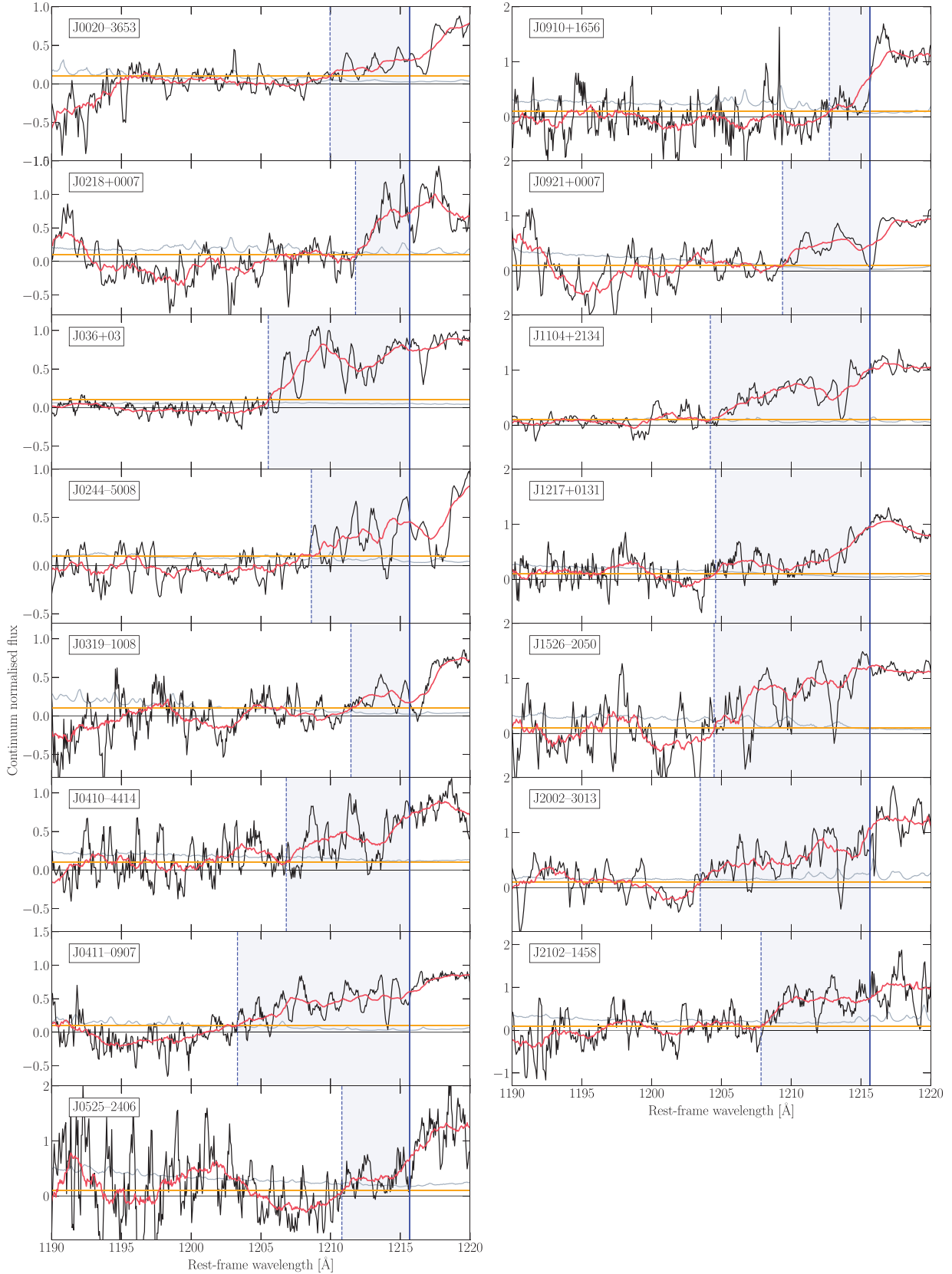
Figure 4. The continuum-normalized spectra and proximity zones of the quasar data set. The black and grey curves display the flux and its noise vector, respectively, both smoothed with a boxcar function of width 5 pixels. The red curve shows the continuum-normalized spectra smoothed with a boxcar function of width 20 Å. As per the definition adopted in the literature, the proximity zone extent is where this curve drops below the 10 per cent flux level (yellow horizontal line). The proximity zone is shown as the shaded blue region, with the Lyα emission line shown as the solid blue vertical line and the proximity zone edge as the dashed blue vertical line.
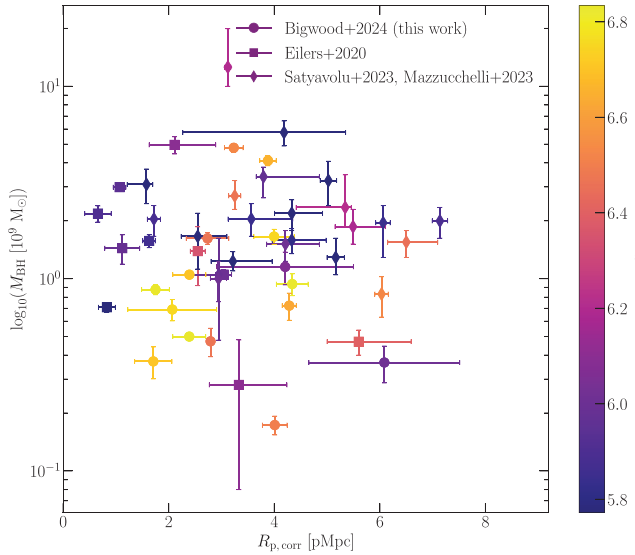
Figure 5. Distribution of quasars in the plane of black hole mass and luminosity-corrected proximity zone size. The FIRE quasar samples of this work are shown by the circle markers. We also plot the measurements of Eilers et al. (2020) (square markers) and Satyavolu et al. (2023b) and Mazzucchelli et al. (2023) (diamond markers).

this work (Fig. 5), we do not expect to find quasar lifetimes correlated with black hole masses in future studies.

ACKNOWLEDGEMENTS

DATA AVAILABILITY

The reduced spectroscopic data are publicly available in Ďurovčíková et al. (2024). The data reduction pipeline PYPEIT is open source.

REFERENCES

Adelberger K. L., 2004, ApJ, 612, 706
Bañados E., Decarli R., Walter F., Venemans B. P., Farina E. P., Fan X., 2015, ApJ, 805, L8
Bennett J. S., Sijacki D., Costa T., Laporte N., Witten C., 2024, MNRAS, 527, 1033
Bochanski J. J. et al., 2009, PASP, 121, 1409
Carilli C. L. et al., 2010, ApJ, 714, 834
Clough S. A., Shephard M. W., Mlawer E. J., Delamere J. S., Iacono M. J., Cady-Pereira K., Boukabara S., Brown P. D., 2005, J. Quant. Spectrosc. Radiat. Transfer, 91, 233
Davies F. B. et al., 2018, ApJ, 864, 143
Davies F. B., Hennawi J. F., Eilers A.-C., 2019, ApJ, 884, L19
Davies F. B., Hennawi J. F., Eilers A.-C., 2020, MNRAS, 493, 1330
Decarli R. et al., 2018, ApJ, 854, 97
Ďurovčíková D. et al., 2024, preprint (arXiv:2401.10328)

Eilers A.-C., Davies F. B., Hennawi J. F., Prochaska J. X., Lukić Z., Mazzucchelli C., 2017, ApJ, 840, 24
Eilers A.-C. et al., 2020, ApJ, 900, 37
Eilers A.-C., Hennawi J. F., Davies F. B., Simcoe R. A., 2021, ApJ, 917, 38
Fan X. et al., 2006, AJ, 132, 117
Fan X., Banados E., Simcoe R. A., 2023, ARA&A, 61, 373
Farina E. P. et al., 2022, ApJ, 941, 106
Foreman-Mackey D., Hogg D. W., Lang D., Goodman J., 2013, PASP, 125, 306
Greig B., Mesinger A., McGreer I. D., Gallerani S., Haiman Z., 2017, MNRAS, 466, 1814
Haiman Z., Hui L., 2001, ApJ, 547, 27
Horne K., 1986, PASP, 98, 609
Khrykin I. S., Hennawi J. F., McQuinn M., Worseck G., 2016, ApJ, 824, 133
Kormendy J., Richstone D., 1995, ARA&A, 33, 581
Lynden-Bell D., 1969, Nature, 223, 690
Martini P., Weinberg D. H., 2001, ApJ, 547, 12
Mazzucchelli C. et al., 2017, ApJ, 849, 91
Mazzucchelli C. et al., 2023, A&A, 676, A71
Miralda-Escudé J., 1998, ApJ, 501, 15
Morey K. A., Eilers A.-C., Davies F. B., Hennawi J. F., Simcoe R. A., 2021, ApJ, 921, 88
Mortlock D. J. et al., 2011, Nature, 474, 616
Novak G. S., Ostriker J. P., Ciotti L., 2011, ApJ, 737, 26
Pâris I. et al., 2011, A&A, 530, A50
Planck Collaboration XIII, 2016, A&A, 594, A13
Prochaska J. X. et al., 2020a, pypeit/PypeIt: Release 1.0.0, Zenodo, https://doi.org/10.5281/zenodo.3743493
Prochaska J. et al., 2020b, J. Open Source Softw., 5, 2308
Reed S. L. et al., 2017, MNRAS, 468, 4702
Reed S. L. et al., 2019, MNRAS, 487, 1874
Richstone D. et al., 1998, Nature, 385, A14
Salpeter E. E., 1964, ApJ, 140, 796
Satyavolu S., Kulkarni G., Keating L. C., Haehnelt M. G., 2023a, MNRAS, 521, 3108
Satyavolu S. et al., 2023b, MNRAS, 522, 4918
Schawinski K., Koss M., Berney S., Sartori L. F., 2015, MNRAS, 451, 2517
Schindler J.-T. et al., 2020, ApJ, 905, 51
Simcoe R. A., Sullivan P. W., Cooksey K. L., Kao M. M., Matejek M. S., Burgasser A. J., 2012, Nature, 492, 79
Soltan A., 1982, MNRAS, 200, 115
Suzuki N., Tytler D., Kirkman D., O'Meara J. M., Lubin D., 2005, ApJ, 618, 592
Tsuzuki Y., Kawara K., Yoshii Y., Oyabu S., Tanabé T., Matsuoka Y., 2006, ApJ, 650, 57
Vestergaard M., Osmer P. S., 2009, ApJ, 699, 800
Vestergaard M., Wilkes B. J., 2001, ApJS, 134, 1
Volonteri M., 2012, Science, 337, 544
Wang F. et al., 2017, ApJ, 839, 27
Wang F. et al., 2020, ApJ, 896, 23
Wang F. et al., 2021, ApJ, 907, L1
Willott C. J. et al., 2007, AJ, 134, 2435
Wu X.-B. et al., 2015, Nature, 518, 512
Yang J. et al., 2019, AJ, 157, 236
Yang J. et al., 2020, ApJ, 897, L14
Yang J. et al., 2021, ApJ, 923, 262
Yu Q., Tremaine S., 2002, MNRAS, 335, 965

APPENDIX A: QUALITY OF THE CONTINUUM RECONSTRUCTION

In order to better demonstrate the continuity of the red and blue continuum reconstruction components, and thus the quality of the continuum reconstruction, Fig. A1 enlarges the region $1170\,\text{Å} < \lambda_{rest} < 1350\,\text{Å}$ of Fig. 3 for visual aid.
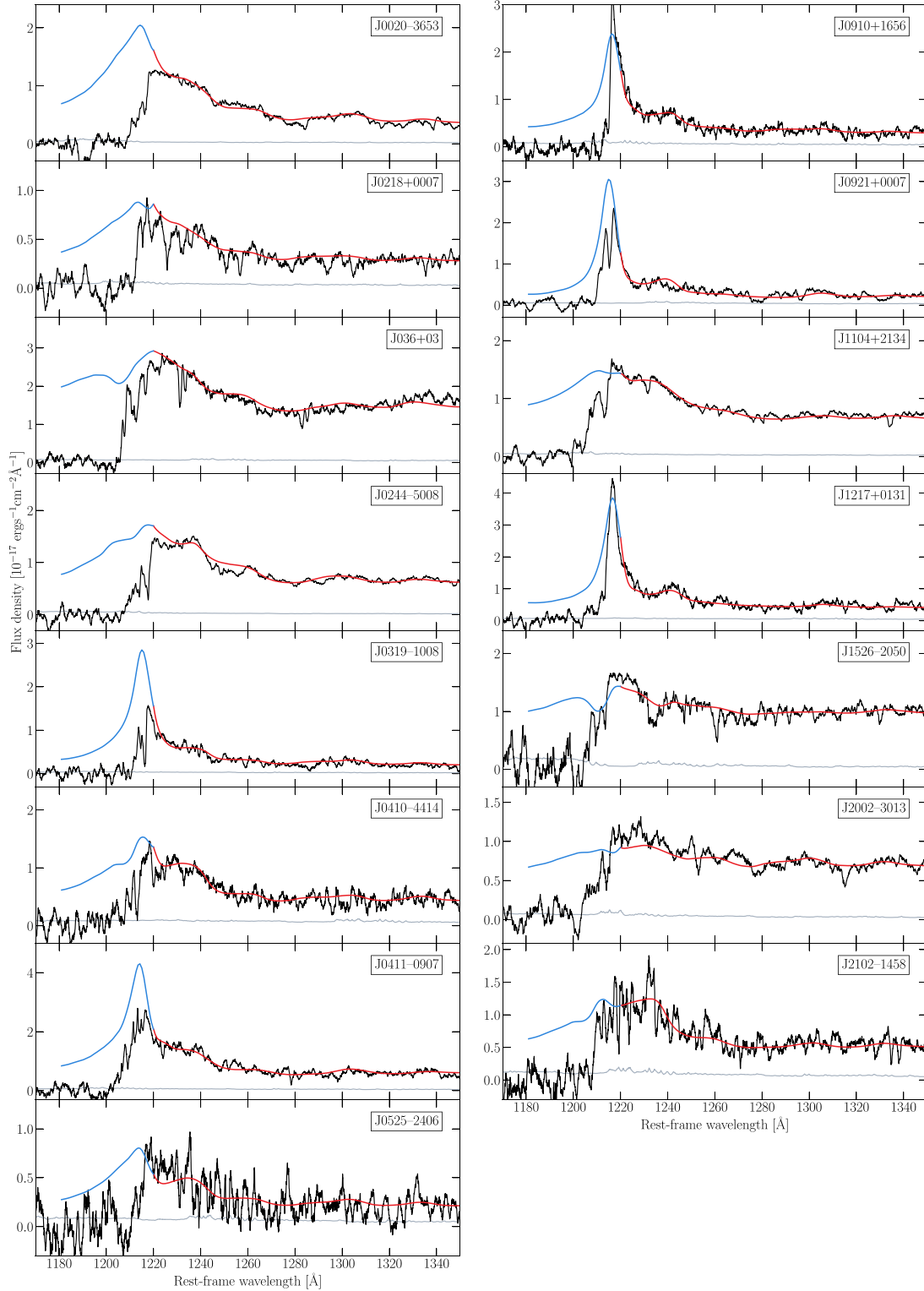
Figure A1. Same as Fig. 3, but enlarging the region showing the continuity between the red and blue continuum reconstruction components, in order to better demonstrate the quality of the reconstruction. We only show the objects for which we utilize the continuum reconstruction in the proximity zone analysis.

This paper has been typeset from a TeX/LaTeX file prepared by the author.